

An evaluation of WRF's ability to reproduce the surface wind over complex terrain based on typical circulation patterns

P. A. Jiménez,^{1,2} J. Dudhia,² J. F. González-Rouco,³ J. P. Montávez,⁴
E. García-Bustamante,⁵ J. Navarro,¹ J. Vilà-Guerau de Arellano,⁶ and
A. Muñoz-Roldán⁷

Received 7 January 2013; revised 13 June 2013; accepted 15 June 2013; published 25 July 2013.

[1] The performance of the Weather Research and Forecasting (WRF) model to reproduce the surface wind circulations over complex terrain is examined. The atmospheric evolution is simulated using two versions of the WRF model during an over 13 year period (1992 to 2005) over a complex terrain region located in the northeast of the Iberian Peninsula. A high horizontal resolution of 2 km is used to provide an accurate representation of the terrain features. The multiyear evaluation focuses on the analysis of the accuracy displayed by the WRF simulations to reproduce the wind field of the six typical wind patterns (WPs) identified over the area in a previous observational work. Each pattern contains a high number of days which allows one to reach solid conclusions regarding the model performance. The accuracy of the simulations to reproduce the wind field under representative synoptic situations, or pressure patterns (PPs), of the Iberian Peninsula is also inspected in order to diagnose errors as a function of the large-scale situation. The evaluation is accomplished using daily averages in order to inspect the ability of WRF to reproduce the surface flow as a result of the interaction between the synoptic scale and the regional topography. Results indicate that model errors can originate from problems in the initial and lateral boundary conditions, misrepresentations at the synoptic scale, or the realism of the topographic features.

Citation: Jiménez, P. A., J. Dudhia, J. F. González-Rouco, J. P. Montávez, E. García-Bustamante, J. Navarro, J. Vilà-Guerau de Arellano, and A. Muñoz-Roldán (2013), An evaluation of WRF's ability to reproduce the surface wind over complex terrain based on typical circulation patterns, *J. Geophys. Res. Atmos.*, 118, 7651–7669, doi:10.1002/jgrd.50585.

1. Introduction

[2] The surface wind field plays a major role in a variety of phenomena operating at the regional scale such as the dispersion of pollutants over a region [Darby, 2005], the production and transport of dust due to wind erosion [Gillette and Hanson, 1989], or the wind resource evaluation [Palutikof et al., 1987; García-Bustamante et al., 2008, 2009]. The surface wind field simulation is therefore an issue of interest for a wide range of applications. General

circulation models (GCMs) can provide adequate results at large scales [von Storch, 1995]. However, when emphasis is placed on resolving shorter spatial scales, results must be interpreted with care since their typical horizontal resolution is not able to capture details of smaller dimension. This limitation can be particularly relevant in complex terrain regions, wherein the surface wind spatial variability can present a high complexity as a consequence of the strong influence that topography produces over the large-scale flows through channeling, forced ascents, blocking, etc. [Whiteman, 2000].

[3] Mesoscale models [e.g., Black, 1994; Grell et al., 1994; Cotton et al., 2003; Skamarock et al., 2008] can be used to overcome the limitations that the GCMs present at the regional scale [von Storch, 1995]. The atmospheric evolution is simulated only over a limited area which allows for a higher horizontal and vertical resolution to provide an improved representation of the regional features [e.g., Rife et al., 2004; Zagar et al., 2006; Conil and Hall, 2006; Jimenez et al., 2013]. These models numerically solve the atmospheric equations of motion using outputs from GCMs as initial and boundary conditions [Pielke, 2002]. During the last decades, a wide range of physical processes have been incorporated in mesoscale model formulation which have considerably increased their complexity. In spite of the more accurate representation of physical processes, simulations need to be compared with the available observations

¹División de Energías Renovables, CIEMAT, Madrid, Spain.

²Mesoscale and Microscale Meteorological Division, NCAR, Boulder, Colorado, USA.

³Departamento de Astrofísica y Ciencias de la Atmósfera, Universidad Complutense de Madrid, Madrid, Spain.

⁴Departamento de Física, Universidad de Murcia, Murcia, Spain.

⁵Department of Geography, Justus-Liebig University of Giessen, Giessen, Germany.

⁶Meteorology and Air Quality Section, Wageningen University, Wageningen, Netherlands.

⁷Unidad de Informática, CIEMAT, Madrid, Spain.

Corresponding author: P. A. Jiménez, División de Energías Renovables, CIEMAT, Avenida Complutense n 40, 28040, Madrid, Spain, and Mesoscale and Microscale Meteorology Division, NCAR, PO Box 3000, Boulder, CO 80307, USA. (jimenez@ucar.edu)

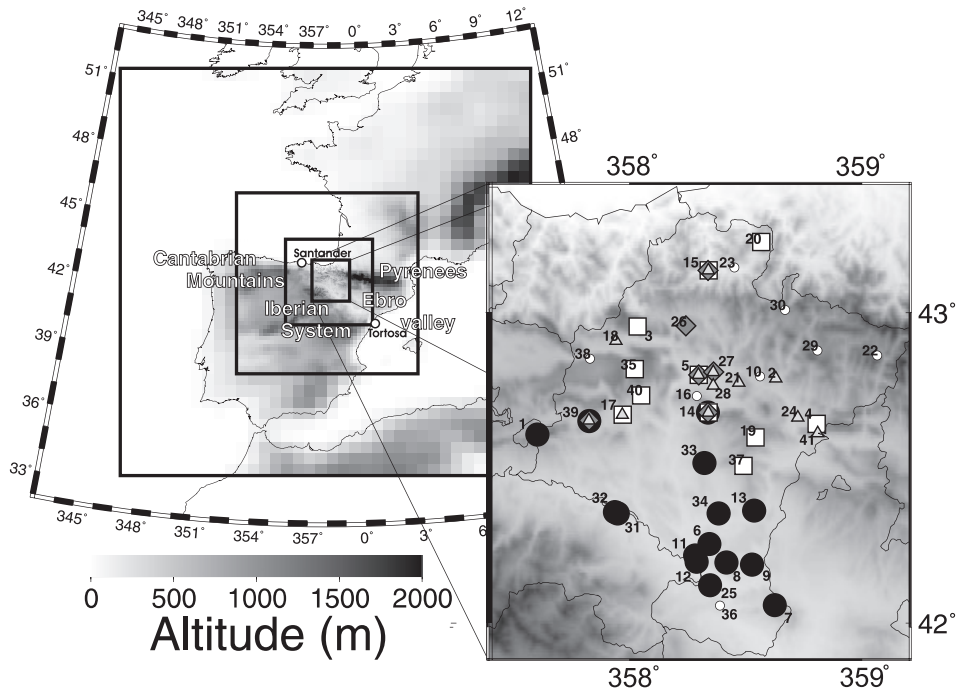


Figure 1. Location of the CFN within the Iberian Peninsula. The left panel highlights the most important geographical features of the Iberian Peninsula and the location of the meteorological stations of Santander and Tortosa. The rectangles represent the four domains used in the WRF simulations showing the topography at their particular horizontal resolutions (54, 18, 6, and 2 km). The right panel shows the regional topography of the CFN and the location of the wind stations used to evaluate the performance of the dynamical downscaling. The different symbols represent the locations that form the subregions with homogeneous wind variability identified by JEA08: Ebro Valley (EV, black circles), mountain stations (MS, squares), north-to-south oriented stations (NS, diamonds), and narrow valleys located to the north of the Ebro Valley (NV, triangles). Additional stations employed in this work which were not classified into a subregion are also displayed (white circles).

in order to ensure that the model is able to reproduce the desired atmospheric characteristics. This is of interest not only to understand the potential errors in a model but also for blending together observations and simulations, in a regional reanalysis for example [e.g., Mesinger *et al.*, 2006], since the existence of biases plays an adverse role in the assimilation process.

[4] The comparison of numerical simulations with observations is usually referred to as “verification” or “validation.” However, verification or validation of numerical models of natural systems can be argued to be impossible in a general sense [Oreskes *et al.*, 1994; Oreskes, 1998]. A simulation can be compared to observations to confirm that the simulation is appropriate for a particular case study inasmuch as it reproduces realistically enough a specific aspect of the real world, but nothing ensures that it will continue to work in other situations. This important limitation inherent to the evaluation of a model performance can only be mitigated by increasing the number of comparisons between observations and simulations. The higher the number of comparisons when the simulation shows an adequate behavior, the more likely that the simulation would perform appropriately in other situations. In this sense, models can only be evaluated in relative terms [Oreskes *et al.*, 1994]. A long temporal period of evaluation is therefore necessary in order to have more confidence in our efforts to generalize the conclusions regarding the performance of a model.

[5] Two limitations have prevented analyzing the mesoscale models performance in reproducing the surface wind behavior during a long temporal period. The first one is the relative scarceness of good quality wind data sets spanning a multiyear period. Some studies have recently contributed to produce quality controlled wind data sets for a number of regions [DeGaetano, 1996; Jiménez *et al.*, 2010b; Fiebrich *et al.*, 2010; McVicar *et al.*, 2012] where performing this kind of evaluations becomes possible. The second one is a technical limitation. Multiyear mesoscale simulations require high computational resources. This problem is aggravated over complex terrain regions since a realistic representation of the topography requires the use of high horizontal resolutions that further increase the computational demand. The computational power reached in the last years is allowing us to perform long simulations at a high horizontal resolution during a year or even multiyear simulations at lower horizontal resolution [e.g., Buckley, 2004; Conil and Hall, 2006; Walter *et al.*, 2006]. However, multiyear simulations performed at a high horizontal resolution are still computationally demanding and have been seldom explored. Therefore, our understanding of the mesoscale simulations’ capability to reproduce the surface wind circulations over complex terrain is still limited. This not only hampers the potential applications of the simulations but also makes it difficult to identify specific aspects in the model formulation that deserve further development.

[6] This study analyzes the ability of a mesoscale model, the Weather Research and Forecasting model (WRF, Skamarock *et al.* [2008]), configured at high horizontal resolution, 2 km, to reproduce the surface wind over complex terrain. The originality of our study consists in analyzing the wind field reproducibility of typical wind fields or wind patterns (WPs) objectively identified with observations acquired during a 13 year period [Jiménez *et al.*, 2009]. Since each pattern is representative of a large number of days, we are able to obtain robust conclusions regarding the performance of the model in reproducing the surface flows that take place under very diverse synoptic conditions (recall the previous discussion of Oreskes [1994, 1998]). An additional advantage is the possibility to discriminate the model's performance in terms of the wind direction. This enables us to extract more precise conclusions than evaluations solely based on the wind speed [e.g., Jiménez and Dudhia, 2012]. The effects that different synoptic situations exert over the surface flow are also investigated in order to determine potential biases introduced under certain situations. For this purpose, the ability of WRF to reproduce the WPs is broken down for typical pressure patterns (PPs) over the region.

[7] The evaluation is performed using daily averages in order to concentrate the investigation in the effects that topography and its interaction with the synoptic scale produce in the surface flow. Hence, our study of the surface wind consists of these three stages: (1) quantify the model's ability to reproduce the surface wind in regions characterized by complex topography; (2) explore the errors as functions of the topographic conditions and the interaction with large-scale flow at the synoptic scale; and (3) diagnose potential misrepresentations arising from the initial and boundary conditions in order to quantify sensitivities in the surface wind simulation related to uncertainties in the synoptic situation. The methodology adopted allows to reach solid conclusions in identifying which parts of the model formulation should be inspected in the future in order to obtain more accurate surface wind simulations with the WRF model.

[8] The manuscript is organized as follows. The next section summarizes the background and the experimental setup used to evaluate the WRF performance. The numerical experiments are described in section 3. Section 4 presents the results of the evaluation that are further extended in section 5 in order to explore the wind field reproducibility as a function of the synoptic situation. Finally, the conclusions are presented in section 6.

2. Background and Experimental Setup

[9] The region of study is the Comunidad Foral de Navarra (CFN), a complex terrain region located in the northeast of the Iberian Peninsula (Figure 1). The complex topography ensures an interesting interaction with the atmospheric dynamics providing an appropriate framework for the WRF evaluation. The CFN is surrounded by three large mountain systems: the Cantabrian Mountains and the Pyrenees dominate the northern areas, whereas the Iberian System constitutes a natural barrier in the southwest. These last two mountain systems shape the broad Ebro Valley which crosses the CFN from northwest to southeast. As a result, the northern part of the region shows a more complex topography than the lower lands in the southeast.

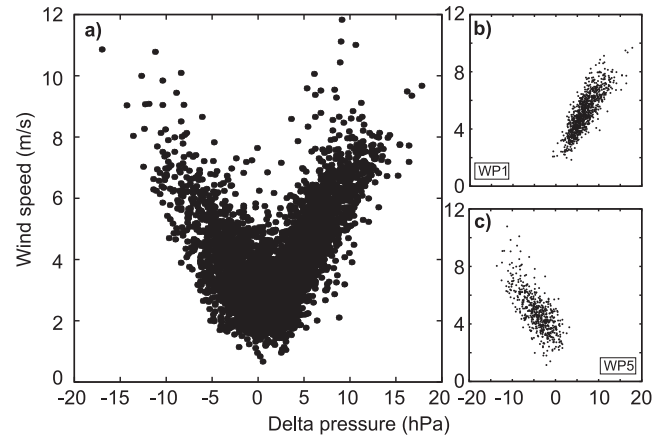


Figure 2. Scatter diagram of the pressure differences along the Ebro Valley and the mean wind speed field, calculated with the records acquired at the 41 observational sites (Figure 1), for (a) the complete data set, (b) days classified as WP1, and (c) days classified as WP5. WP1 shows strong northwestern circulations, whereas WP5 reveals strong southeastern flows (JEA09). The pressure difference is defined as the SLP observed at Santander minus its corresponding value at Tortosa (Figure 1).

[10] The existence of a reasonably long period (1992–2005) with quality controlled wind data at 41 observational sites [Jiménez *et al.*, 2010b] as well as a distribution of stations that cover quite different locations (e.g., plains, valleys, mountain tops, hills, etc.) makes the area suitable for the purposes of this investigation. Previous observational works have provided a statistically robust characterization of the prevailing surface flows, the WPs [Jiménez *et al.*, 2009, JEA09 hereafter], and the daily wind variability [Jiménez *et al.*, 2008, JEA08 hereafter], and their results will serve as a base for the evaluation exercise of the present investigation. JEA09 analyzed the dominant surface flows over the CFN by grouping daily mean fields, represented by observations at 41 observational sites (Figure 1), into groups of typical WPs. A total of six WPs were identified applying a cluster analysis procedure based on the spatial similarity of the wind fields [Kaufmann and Whiteman, 1999]. Five WPs display a northwest-southeast direction of the flow (91.4% of the days), and one WP shows southwestern wind (8.6% of the days). This result revealed the strong influence of the topography over the surface flows since the most important valleys in the CFN exhibit a NW-SE orientation (Figure 1).

[11] The sea level pressure (SLP) fields over the Iberian Peninsula were also classified by JEA09 and related to the already identified WPs in order to understand the large-scale modes that generate regional variability. A methodology based on principal components and cluster analysis [e.g., Romero *et al.*, 1999] was used to identify a total of eight representative PPs using the SLP from the ERA-40 reanalysis [Uppala *et al.*, 2005]. The relationships found between the PPs and the WPs revealed the importance of the intensification of the flow exerted by the pressure gradient along the valleys. Higher pressures in the Atlantic in comparison with the ones over the Mediterranean Sea favor northwestern winds over the CFN, whereas negative pressure gradients and higher pressures in the Mediterranean intensify

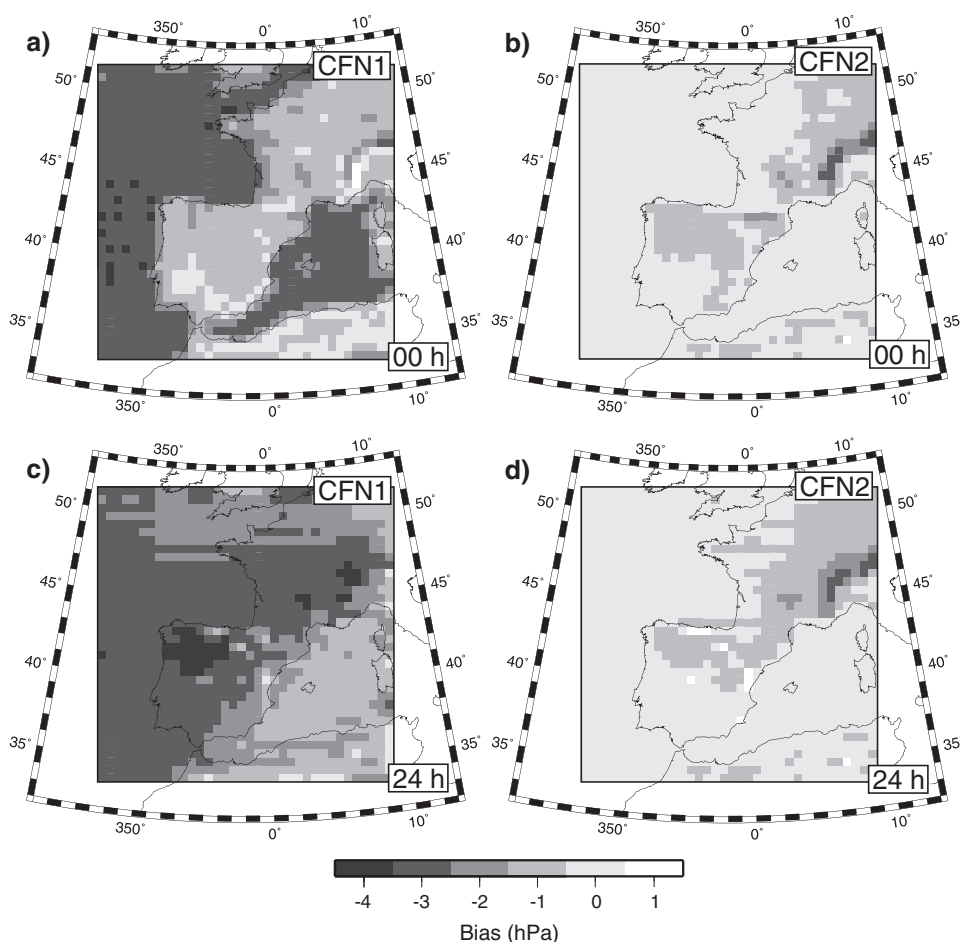


Figure 3. SLP bias calculated with the (a, b) initial conditions as well as (c, d) at 24 h of simulation for CFN1 (Figures 3a and 3c) and CFN2 (Figures 3b and 3d). The ECMWF data used as initial and boundary conditions are used to calculate the biases. The bias is defined as the SLP from the outermost WRF simulations minus the SLP from the ECMWF data sets.

the winds up the Ebro Valley (JEA09). As an illustration of the importance of this mechanism, Figure 2a shows the dispersion diagram between the observed wind speed over the region and the pressure difference along the Ebro Valley. The pressure differences are calculated from daily mean SLP observations at Santander, located at the headboard of the Ebro Valley, minus the pressure at Tortosa, located at the valley mouth (Figure 1, approximately 600 km). There is a direct relationship between the mean wind speed in the region and the absolute value of the pressure difference ($r = 0.76$). The dispersion diagrams for days classified as the northwestern flow of WP1 (Figure 2b) and the southeastern flow of WP5 (Figure 2c) clearly show that the positive pressure differences intensify the northwestern winds, whereas the negative differences intensify the southeastern ones. The ability of a simulation to reproduce this pressure gradient is therefore critical for an adequate surface wind simulation over the CFN.

[12] In an independent observational study, JEA08 analyzed the daily wind variability at the CFN by grouping together the observational sites with similar temporal variability and, thus, identifying subregions of coherent wind behavior. A total of four regions were identified using a classification methodology based on the rotation of the most

important modes of variation from a principal component analysis [White *et al.*, 1991]. The wind subregions found are in general agreement with the topography over the area (Figure 1): a first subregion is formed by stations located in the Ebro Valley (EV subregion, black circles in Figure 1); another group is mainly formed by mountain stations (MS subregion, squares); a third subregion consists of several stations with a north-to-south or meridional orientation in central areas of the CFN (NS subregion, diamonds); and the last group is mainly formed by stations located in the narrow valleys to the north of the Ebro Valley (NV subregion, triangles). A previous WRF simulation that spans the 13 years of the observational period at a high horizontal resolution, 2 km, over the CFN has been shown by Jiménez *et al.* [2010a] to reproduce the wind variability at the four wind regions. The study illustrates the realism of WRF in reproducing areas of coherent variability of surface wind over the CFN. This simulation will be labeled as CFN1 hereafter.

[13] The long-term biases in the wind speed of CFN1 were analyzed by Jiménez and Dudhia [2012, JD12 hereafter]. JD12 found a systematic overestimation of the wind speed over the valleys and an underestimation at the mountain tops and hills. The biases were attributed to limitations

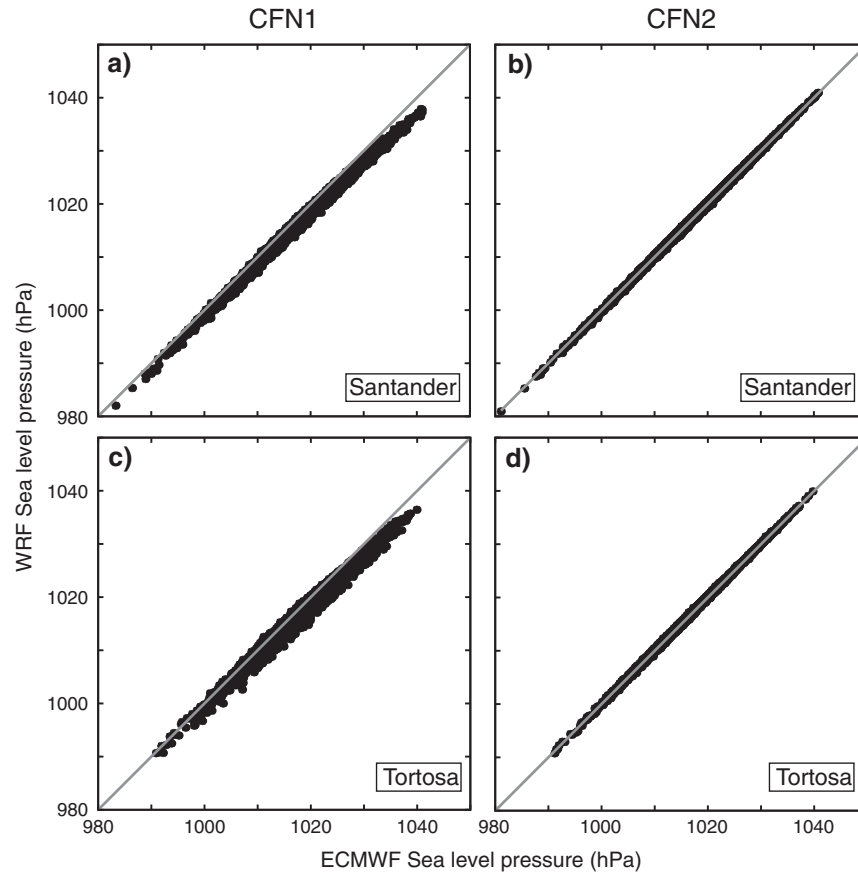


Figure 4. Scatter diagram of the SLP from the WRF initial conditions versus SLP from the ECMWF data sets at (a, b) Santander and (c, d) Tortosa (see Figure 1 for the location of these sites).

in the topographic representation that occur even using 2 km of horizontal resolution which can be considered high. Improvements in the WRF formulation were introduced by JD12 to correct for both kinds of biases. However, the analysis there was focused on the wind module and the effects of the wind direction were neglected in the investigation of JD12.

[14] The present investigation analyzes the ability of WRF to reproduce the flow of the six WPs identified by JEA09, and therefore this assessment does not only consider wind speed but it also takes into account the direction of the flow in the evaluation of the model's performance. For this purpose the CFN1 simulation will be used. It will be herein shown that CFN1 presents a problem in the initial and boundary conditions as a consequence of an inadequate initialization of the surface pressure (see section 3) which introduces errors in the surface wind simulation over the CFN. To overcome this limitation and provide a more reliable evaluation of the WRF model, a new simulation has been performed with identical settings as in CFN1 but solving the problem in the surface pressure of the initial and boundary conditions. This second WRF simulation will be labeled as CFN2 hereafter. By comparing results from these two simulations, we are able to inspect sensitivities of the wind at the regional scale to errors or uncertainties at the synoptic scale.

[15] In order to provide a detailed evaluation of the WRF capability to reproduce the influence of the topography, the

analysis over each WP is broken down for the four wind sub-regions (Figure 1). The evaluation over areas with similar daily wind variability, instead of at site level, provides certain advantages in the evaluation of numerical simulations, such as the mitigation of local effects in the observations or the representativeness of the grid point used for comparison [Reid and Turner, 2001; Jiménez et al., 2010a]. Since the target of a mesoscale simulation is to obtain details of the atmospheric evolution at the regional scale from large-scale fields, the last step of the evaluation consists of analyzing the performance of WRF in reproducing the surface wind field as a function of the synoptic situation. With this aim, the WRF's ability to reproduce each WP will be evaluated separately for each one of its associated PPs.

[16] Hence, the present work extends the observational studies of JEA08 and JEA09 to provide a statistically robust evaluation of the simulation performance in reproducing the surface wind and thus complements the previous evaluation of the ability of WRF to reproduce the wind variability [Jiménez et al., 2010a] and the long-term wind speed (JD12), adding information on the ability of the model to reproduce the surface wind field and its dependence on the synoptic scale. We therefore inspect our previous numerical data set, CFN1, with a different perspective, evaluating the reproducibility of typical wind patterns over the region. A new simulated data set is also created, CFN2, which contributes to progress in our understanding of the ability of WRF to reproduce the wind field.

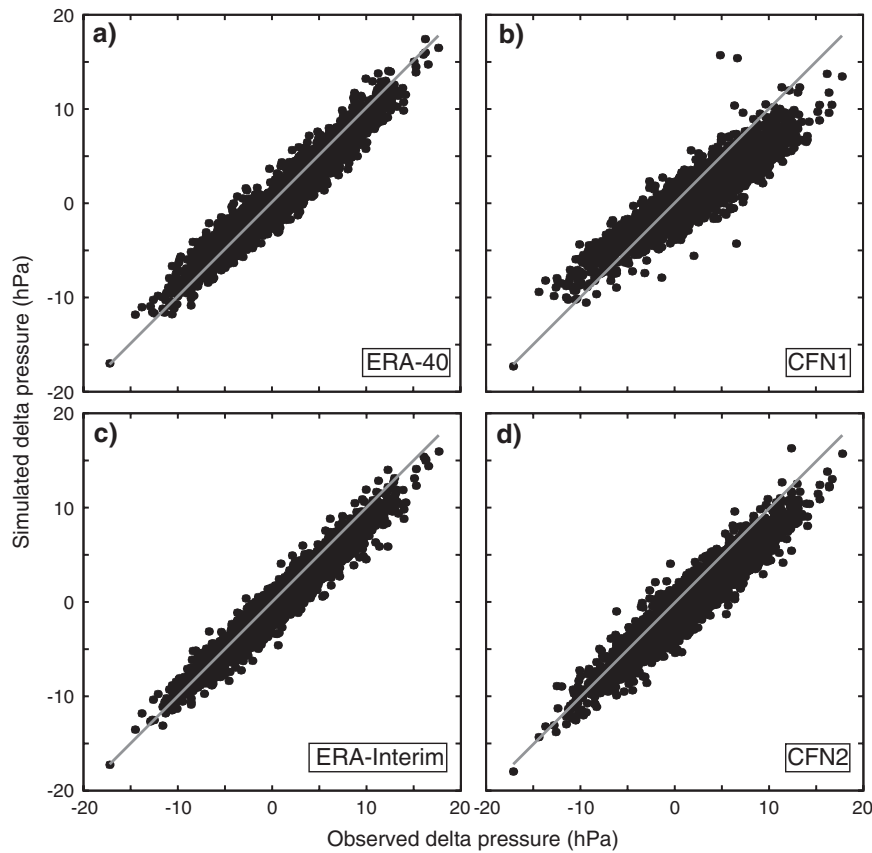


Figure 5. Scatter diagram of the pressure difference calculated with observations versus the pressure difference calculated with (a) ERA-40, (b) CFN1, (c) ERA-Interim, and (d) CFN2. SLP from the outermost domain is used for CFN1 and CFN2.

3. WRF Numerical Simulations

[17] Both regional simulations CFN1 and CFN2 have been accomplished with the WRF mesoscale model. The simulations are summarized in the following lines. A more in-depth discussion of the dynamical and physical settings can be found in Jiménez *et al.* [2010a], where the interested reader is referred to obtain further information. The WRF model is configured with four two-way interacting nested domains (Figure 1) in order to reach a horizontal resolution of 2 km over the CFN. A total of 31 vertical levels, 10 of them distributed within the planetary boundary layer, are prescribed in the simulations. The initial and boundary conditions necessary to perform the numerical simulations were obtained from the European Centre for Medium-Range Weather Forecasts (ECMWF) reanalysis/analysis data sets. The regional simulations consist of a sequence of short runs of the WRF model. Each model run is initialized at the 0:00 h of each day and is run for 48 h. The first 24 h are discarded as model spin-up, and the wind at 10 m above ground level for the following 24 h is averaged to obtain the daily mean wind speed and direction for that day. The spin-up therefore consists of a full diurnal cycle in order to consider both the processes that develop under stable and unstable situations to the model adjustments. The process is repeated until obtaining one simulation for the 5028 days that comprise the observational period (1 January 1992 to 6 October 2005). WRF diagnoses the wind at 10 m using the Monin-

Obukhov similarity theory to extrapolate the wind from the first model level (approximately 28 m in this simulation), which is assumed to represent the atmospheric surface layer [Jiménez *et al.*, 2012].

[18] The main difference between CFN1 and CFN2 lies in the version of the WRF model. CFN1 was performed with WRF version 2.1.2 [Skamarock *et al.*, 2005], whereas CFN2 used WRF version 3.1.1 [Skamarock *et al.*, 2008]. Furthermore, CFN1 and CFN2 differ in the data used as initial and boundary conditions. CFN1 uses data from the ERA-40 reanalysis project [Uppala *et al.*, 2005] until August 2002. Afterward, data from the operational analysis at ECMWF is used. Both ERA-40 and the analysis have a spatial resolution of $1 \times 1^\circ$. On the contrary, CFN2 uses data from the ERA-Interim reanalysis project [Dee *et al.*, 2011], at a horizontal resolution of $0.75 \times 0.75^\circ$ during the complete simulation period. Aside from these differences, both simulations were configured using the same physical and dynamical settings. The interested reader is referred to Skamarock *et al.* [2005, 2008] for a detailed description of the WRF's computation of the ICs as well as the BCs.

[19] The limitation in the initial and boundary conditions of CFN1 can be appreciated in Figure 3, which shows the SLP bias at the initialization time and at 24 h later calculated with the WRF simulations of CFN1 and CFN2, and the ECMWF data used to initialize the numerical experiments. CFN1 shows a negative bias especially clear over both

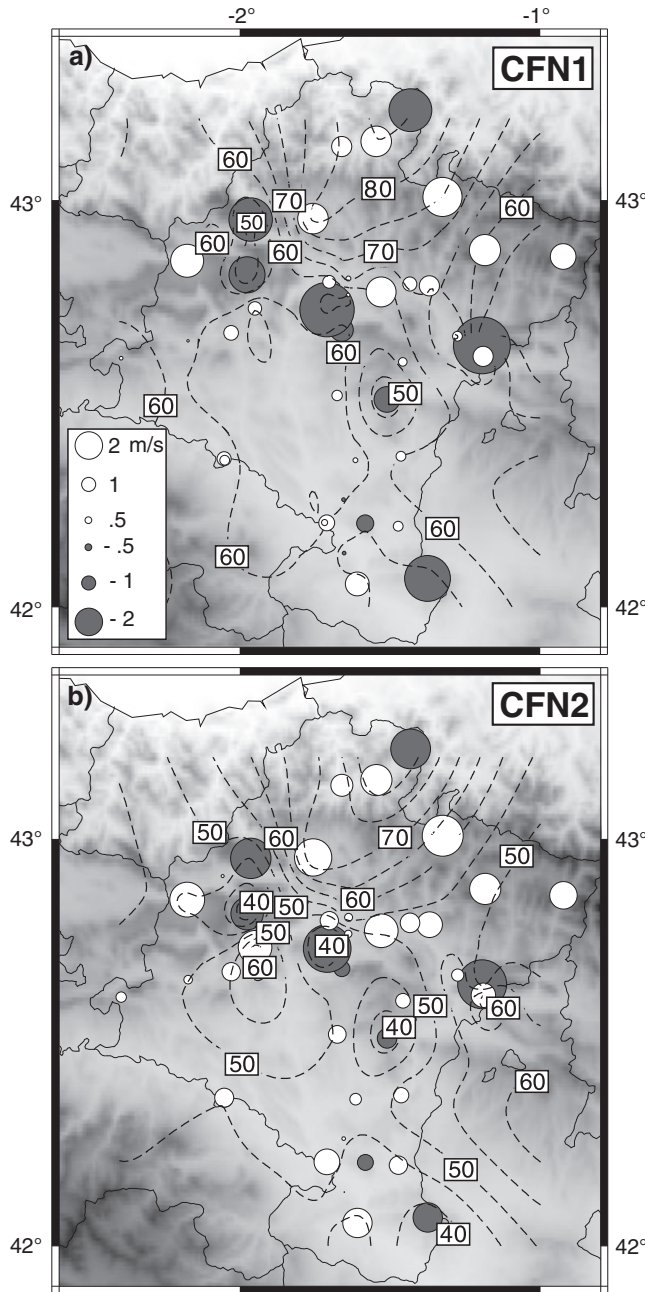


Figure 6. Wind speed bias (circles) and RMSE of the wind direction (contour lines) calculated with (a) CFN1 and (b) CFN2. The wind speed bias is defined as the mean simulated wind speed minus the mean observed wind speed. The radius of the circles is proportional to the magnitude of the bias, and the white (gray) color denotes positive (negative) values.

the Atlantic Ocean and the Mediterranean Sea (Figure 3a). The bias is practically absent in the initialization of CFN2 (Figure 3b). There are only some discrepancies over the mountains, and these seem to be related to the diagnosis of the pressure under the terrain features. The underestimation of the pressure in CFN1 is a result of the initialization of the surface pressure (SP) from the lowest geopotential level, 1000 hPa, when the SP is higher than 1000 hPa. For this purpose an extrapolation formula based on empirical considerations was used by the model version 2.1.2. CFN2 does

not show this bias because the updated version of WRF used in this simulation uses the SLP from reanalysis to initialize the SP. The biases in CFN1 are larger over the ocean because the SP is higher there and the extrapolation formula is used more often than over land, where interpolation between two geopotential heights (such as 1000 hPa and 850 hPa) is more frequent in the initialization of the SP. The empirical formula used to initialize the SP is less accurate for higher SPs and tends to produce a higher underestimation, which also contributes to the higher discrepancies found over the ocean (Figure 3a). This is illustrated in the scatter plot of the SLP from ECMWF and the WRF initial SLP at Tortosa and Santander (Figure 4). The underestimation of the SLP becomes evident for CFN1, especially clear for the higher SLP values (Figures 4a and 4c). On the contrary, CFN2 does not show these systematic errors (Figures 4c and 4d). CFN1 reveals a considerably larger scatter at both locations in comparison with CFN2 also associated with the use of the empirical approximation.

[20] The limitations in the initialization that occur in CFN1 are still noticeable 24 h later (Figure 3c). However, the bias over the Mediterranean Sea is about 2 hPa weaker than at the initialization time (Figure 3a). This is a consequence of the effects produced by the boundary conditions. The boundaries in the eastern part of the domain are mainly located over land, and the errors associated with the calculation of the SP are smaller than those in the Atlantic, where the boundaries are located over the ocean and thus present the same limitations as for the initialization step. Therefore, the more accurate boundary conditions in the eastern part of the domain partially compensate the initialization problems. As a result of these different biases in the Atlantic Ocean and in the Mediterranean Sea, there is an underestimation of the pressure gradient over the Ebro Valley (Figure 3c). CFN2 does not suffer from any influence associated with these problems in the boundary conditions (Figure 4d).

[21] The limitations of CFN1 to reproduce the observed pressure difference over the Ebro Valley are better appreciated in the scatter plot of the observed pressure difference and the difference from the simulated data sets (Figure 5). Both reanalysis, ERA-40, and ERA-Interim show noticeable scatter but in a general good agreement with observations (Figures 5a and 5c). The CFN1 simulation also shows noticeable scatter but more important than that is an underestimation of the absolute value of the pressure difference due to underestimating high pressures as a consequence of the problems in the initialization (Figure 5b). CFN2 shows a much better agreement with observations, especially for negative pressure differences (Figure 5d). The positive pressure differences are somewhat underestimated. A closer look reveals that this was already noticeable in the ERA-Interim data used as initial and boundary conditions (Figure 5c). It will be shown that the limitations to reproduce the pressure difference in CFN1, and to a lesser extent in CFN2, translate into limitations in reproducing the surface wind over the CFN.

[22] The observed wind at the 41 sites that define the WPs is compared with the simulations at the nearest grid points to the observational sites. This representation has been adopted in several studies [e.g., Cox *et al.*, 1998; Hanna and Yang, 2001; Buckley, 2004; Miao *et al.*, 2008], and it is here selected due to its simplicity. Some limitations of this

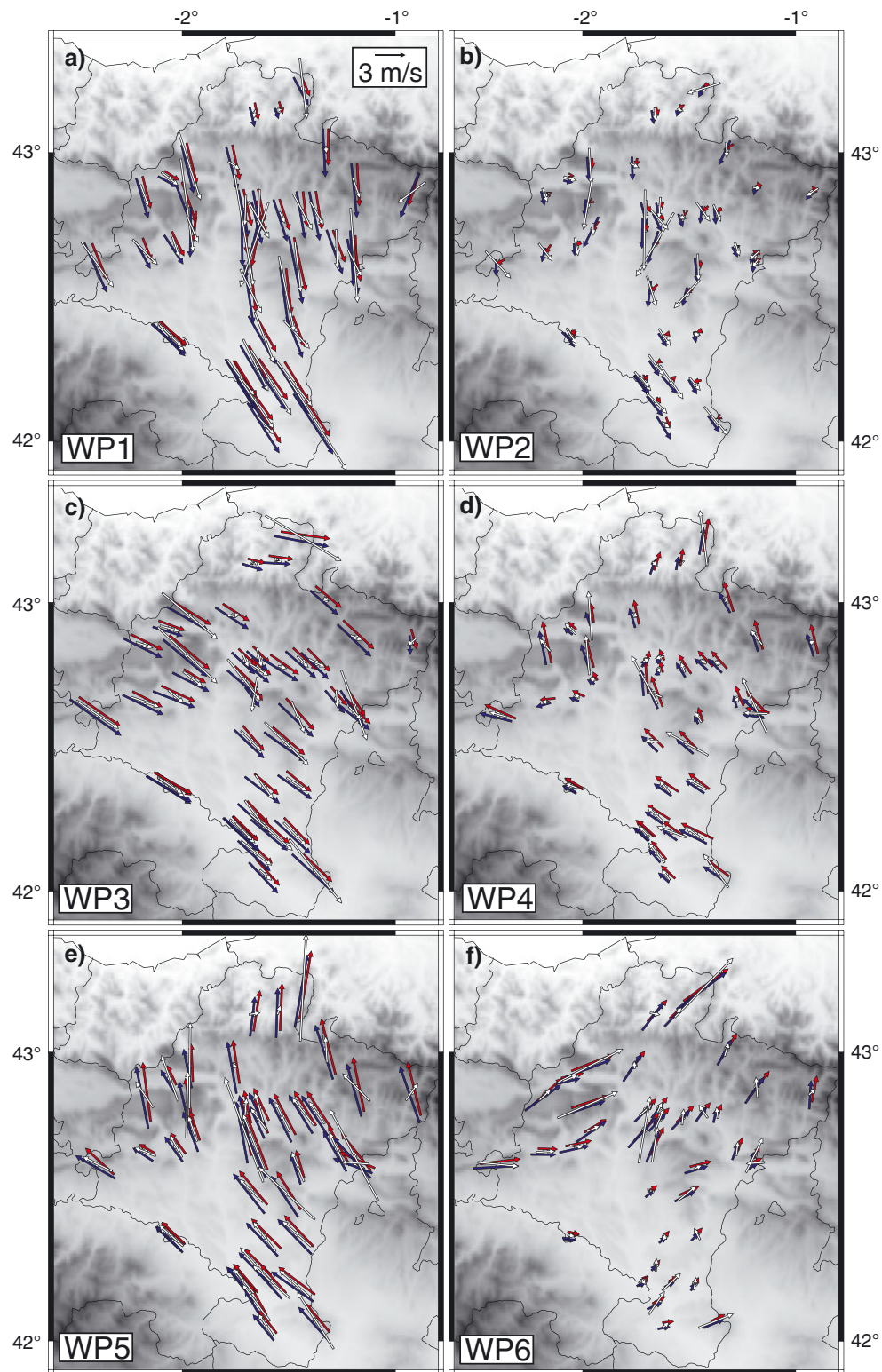


Figure 7. Mean wind vectors calculated with the observations (white arrows), CFN1 (red arrows), and CFN2 (blue arrows) for all days classified as (a) WP1, (b) WP2, (c) WP3, (d) WP4, (e) WP5, and (f) WP6.

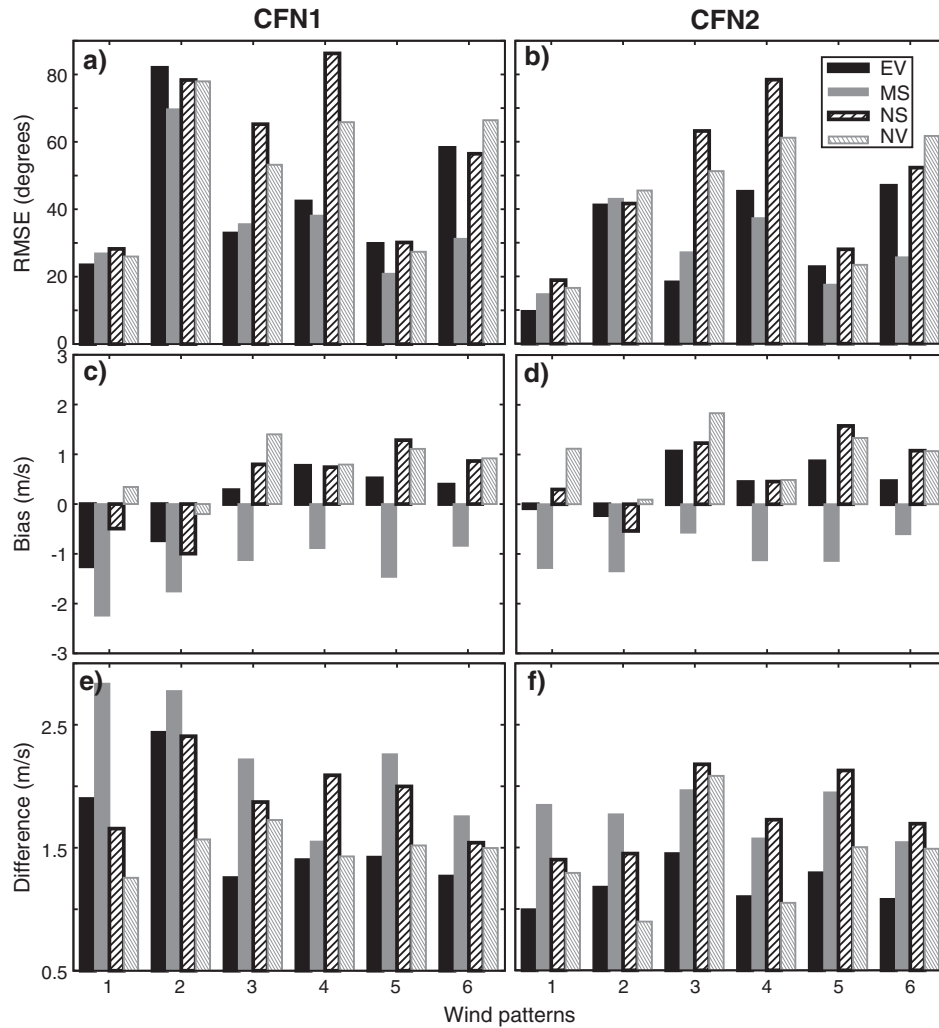


Figure 8. (a, b) RMSE of the wind direction, (c, d) wind speed bias, and (e, f) vectorial wind differences calculated with the observed and simulated regional time series for days belonging to each WP. Both results from the CFN1 (in Figures 8a, 8c, and 8e) and CFN2 (in Figures 8b, 8d, and 8f) are shown. The regions with homogeneous wind variability used to calculate the regional time series are defined in Figure 1.

representation for these particular wind data sets are discussed in Jiménez *et al.* [2010a] and JD12. The daily mean wind simulated at 10 m above ground level is used in the comparison since the majority of the wind sensors are situated at this height [Jiménez *et al.*, 2010b]. The few wind records taken at 2 m above ground level (seven stations) were extrapolated to 10 m using the power law with an exponent of $1/7$, as it was done for instance in Pryor *et al.* [2005]. As a final step in the data preparation, the simulated counterparts of missing observations were removed from the 41 simulated time series in order to perform the evaluation with equivalent data sets.

4. Wind Field Reproducibility

[23] As a preliminary inspection of the WRF performance, the long-term behavior of the simulation is evaluated (section 4.1). The discussion highlights the effects of the orography used in the numerical experiment over the simulated wind field. The WRF evaluation is extended by

analyzing the capability of the simulation to replicate the mean flow of the six typical WPs over the CFN (section 4.2). This second comparison discriminates the wind errors as a function of the direction of the flow. Both simulations, CFN1 and CFN2, are compared with observations which allows us to inspect how sensitive is the regional wind simulation to uncertainties in the synoptic scale.

4.1. 13 Year Evaluation

[24] The wind speed bias and the root mean squared error (RMSE) of the direction at each station are shown in Figure 6. The RMSE is calculated using the departure from the observed wind direction in the sense that provides the smaller difference. Both simulations, CFN1 and CFN2, show a similar structure in the bias and RMSE. The wind direction is better reproduced at the mountain tops (stations 3, 4, 16, 20, 35, and 37; Figure 1) than at the valleys likely due to a weaker influence of the surrounding topography on the flow at the former locations. There is a tendency of the simulation to underestimate the wind speed at the

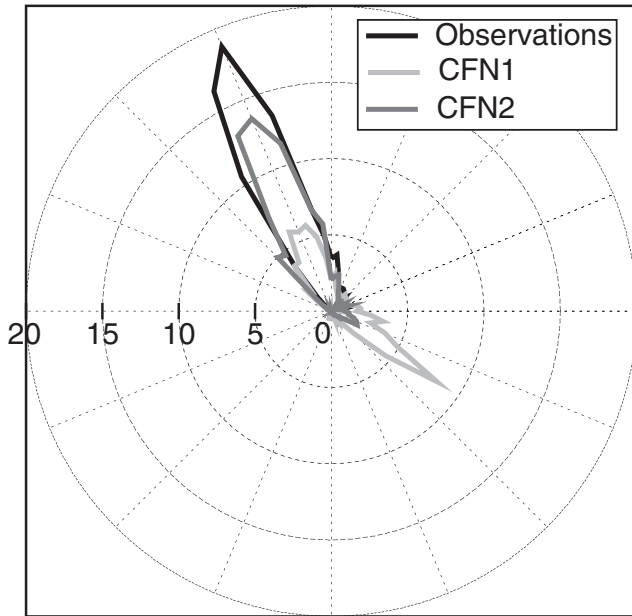


Figure 9. Wind roses at the EV subregion calculated with days classified as WP2 for the observational data set, CFN1, and CFN2 (see legend). The wind rose represents the frequency of occurrence of each wind direction.

windiest observational sites located at mountain tops and the two sites located on hills (stations 7 and 8; Figure 1) and to overestimate it at the less windy areas situated in the valleys. This causes a reduced spatial variability of the simulated wind speed field compared to the observational one already pointed out by JD12. The systematic biases that occur at the mountains and valleys have been attributed by JD12 to the effects produced by the topographic features that are not well resolved in the model. The underestimation at the mountain sites is a result of the underestimation of the mountain heights and upstream influence (JD12). In spite of using 2 km of horizontal resolution in the simulation, the mountains are smoother than reality (hundreds of meters; see Figure 5b in JD12). The smoothed topography is also related to constraints imposed to ensure numerical stability. The underestimation of the mountain height ultimately leads to the underestimation of the wind speed if we assume that mountain sites are well exposed to the geostrophic winds and that the wind speed increases with height in the lower troposphere. Over the valleys and more gentle terrain areas, the overestimation has been attributed by JD12 to the drag generated by the subgrid scale orography. These topographic features produce an additional drag to that one generated by vegetation (the roughness length, z_0), and if their effects are not considered, they could be responsible for the overestimation of the wind speed (JD12). Indeed, this kind of topographic drag has been parameterized in other mesoscale models [e.g., Mesinger *et al.*, 1996; Rontu, 2006], but it is not parameterized in WRF. Other effects such as the filling of the valleys associated with the smoother topography could be partially responsible for the wind speed biases, but their effects are believed to be of smaller magnitude than the factors mentioned above.

[25] A closer examination reveals that the winds are stronger in CFN2 than in CFN1 (Figure 6). The overestimation at the valleys is higher, whereas the underestimation of the wind at the mountain sites is smaller. The higher wind speeds are associated with the higher pressure gradients simulated in CFN2 (Figure 5). A better reproduction of the wind direction in CFN2 than in CFN1 is noticeable. The RMSE is about 10 degrees lower in CFN2. The improvement of the wind direction is related to the better initialization of CFN2 as will be shown in the following section.

4.2. Wind Patterns

[26] The mean observed/simulated wind field of days belonging to each one of the six WPs are displayed in Figure 7. The first three WPs display northwestern wind (Figures 7a–7c), the following WP4 and WP5 (Figures 7d and 7e) reveal southeastern flow, and the last WP6 shows southwestern surface flows (Figure 7f). In general, both CFN1 and CFN2 reproduce the main characteristics of the surface flow structure under the different WPs. The main difference occurs for WP2, where CFN2 shows a remarkable better reproduction of the flow than CFN1 (Figure 7b).

[27] A quantification of the skill displayed by the simulation to reproduce the mean flow under each WP is broken down for the four wind subregions with different wind variability (Figure 1) in Figure 8. The CFN1 simulation shows the best wind direction reproduction in the MS subregion with RMSE under 40 degrees except for WP2, under which the four subregions show poor scores (Figure 8a). The flows along the Ebro Valley are also reasonably well captured as indicated by the moderate RMSE scores at the EV subregion under WP1, WP3, WP4, and WP5, the only exception being WP2 as indicated above. The simulation is less skillful in reproducing the cross Ebro Valley winds of WP6. The other valley subregions, NS and NV, display higher RMSE values than the EV, showing scores around 70 degrees except for the strong winds of WP1 and WP5 (Figures 7a and 7e), under which the four subregions show RMSE below 30 degrees. CFN2 shows a better reproduction of the wind direction for WP2; there is a reduction of 40 degrees in comparison with the RMSE of CFN1 and a more modest improvement of about 10 degrees for WP1 (Figures 8a and 8b).

[28] A better understanding of the different performance to reproduce the wind direction of WP2 by CFN1 and CFN2 becomes evident in the wind roses at the EV subregion calculated with the days classified as WP2 (Figure 9). The simulated wind roses tend to show a principal direction in agreement with the one displayed by the observations. However, the wind rose calculated with CFN1 shows two main directions, one of them opposite to the observed one. Although the wind rose calculated with data from CFN2 shows a better agreement with observations, it still shows certain days with a SE orientation of the flow. The simulation of a surface flow with an opposite sense as the observed case may not be limited to the poor representation of some topographical features. Instead, it appears more likely to be related to a misrepresentation of the large-scale field. To be more concrete, we found that it is related to the underestimation of the pressure gradient over the Ebro Valley that occurs in the WRF simulations (Figures 5b and 5d). The pressure gradient in CFN1 is weaker than observed, and in some cases even negative, which favors the simulation of SE winds

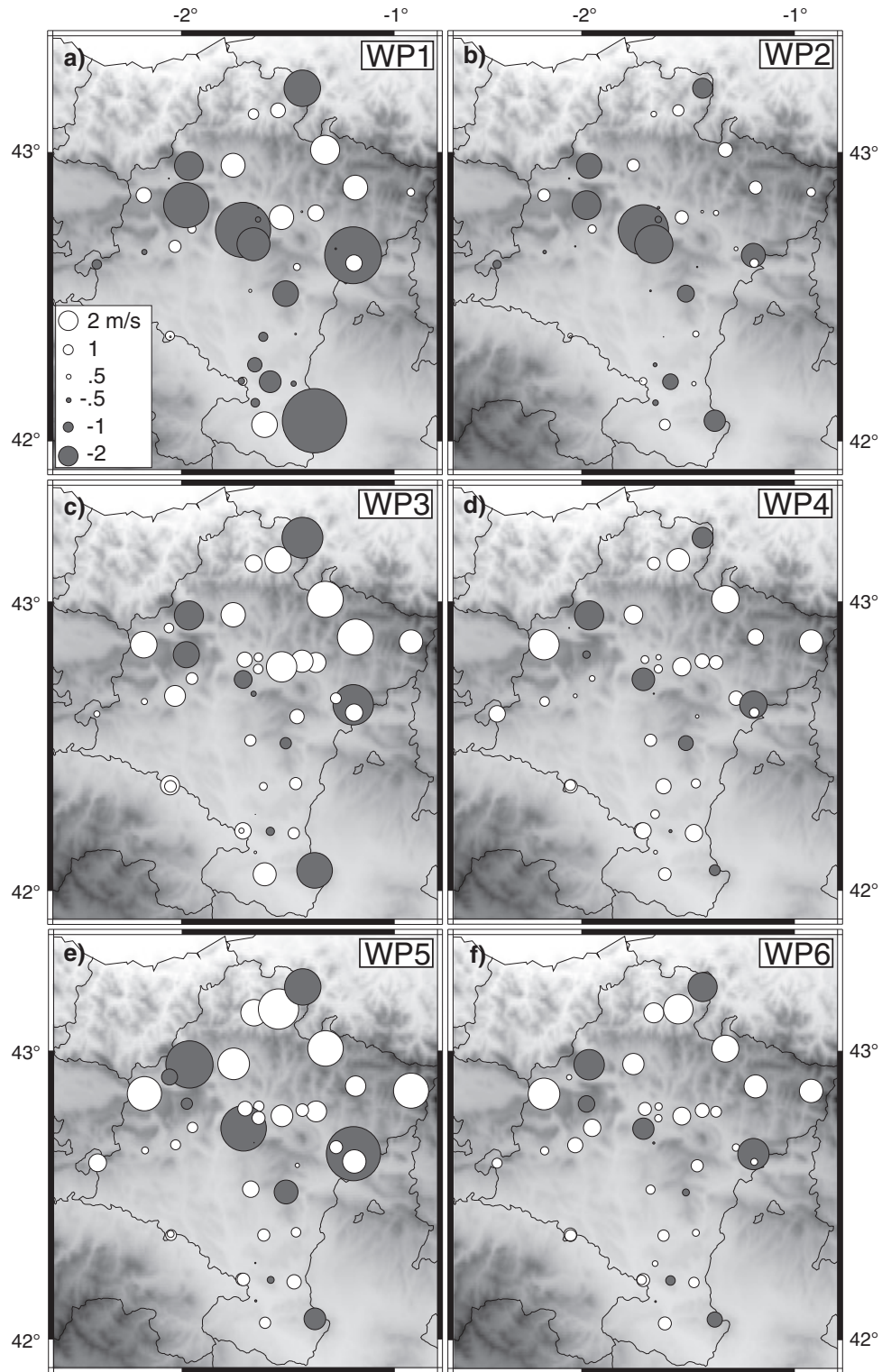


Figure 10. Wind speed biases for days classified as (a) WP1, (b) WP2, (c) WP3, (d) WP4, (e) WP5, and (f) WP6. The wind speed from CFN1 is used in the comparison.

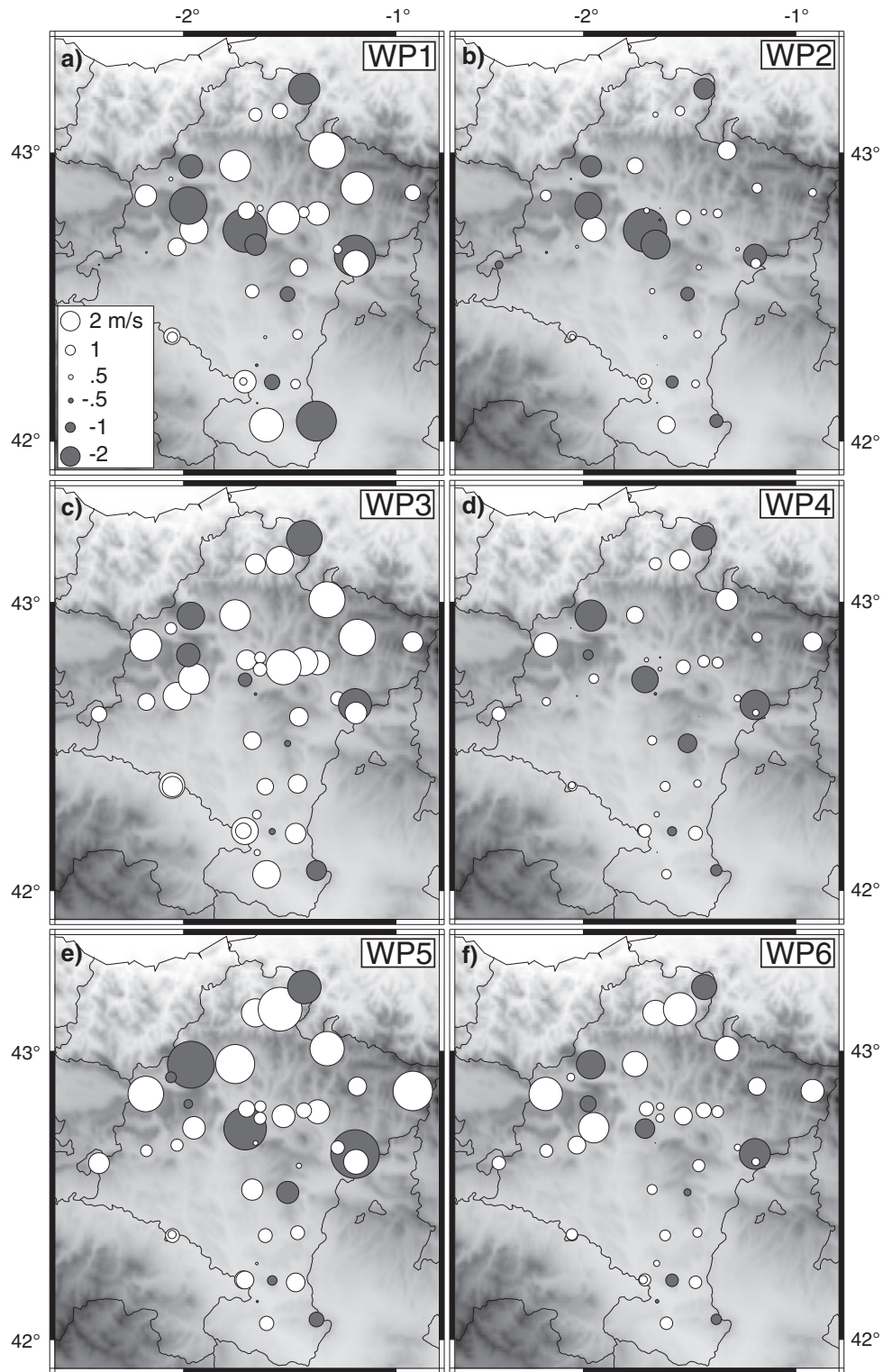


Figure 11. Same as Figure 10 but for CFN2.

instead of the NW flow typical of WP2. CFN2 still suffers from some limitations due to the slight underestimation of positive gradients (Figure 5d).

[29] The attribution of the errors in the wind direction that occur in WP2 to the initialization process of CFN1 is supported by an additional WRF numerical experiment wherein we use the same settings as in CFN2 but we initialize the

SP using an extrapolation from the lowest geopotential level (1000 hPa) like in CFN1. The comparison of results from this experiment, labeled as CFN2.1, and CFN2 allows us to isolate the errors associated with the initialization process. The new simulation spans only 3 years (2001–2003) but is able to reproduce the large RMSE value that occurs in WP2 in the CFN1 simulation (Figure 8a).

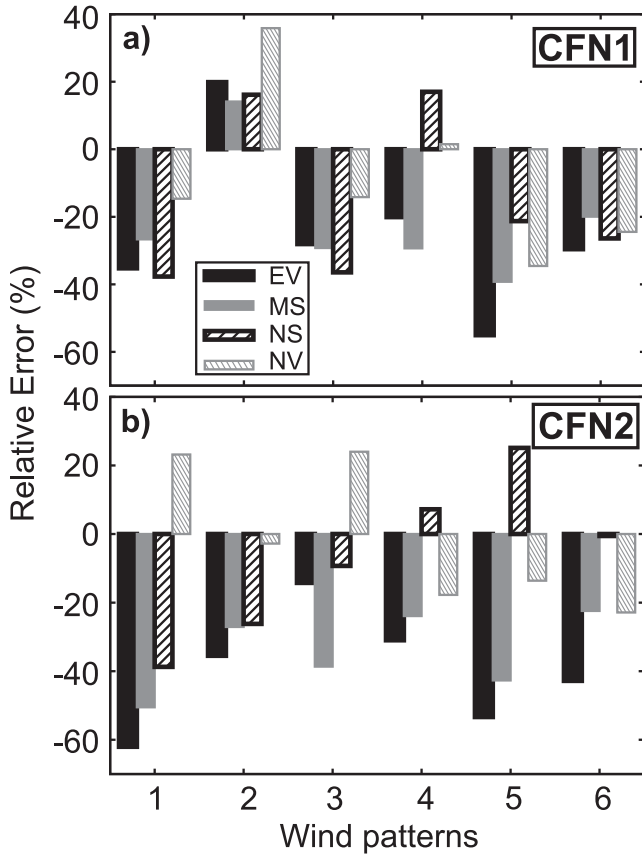


Figure 12. Relative error [equation (2)] between (a) CFN1 and ERA-40 and (b) CFN2 and ERA-Interim for the different WPs and wind regions (see legend).

[30] The winds over the mountain stations (MS) are systematically underestimated by both simulations (Figures 8c and 8d). The wind speed at the valley subregions (EV, NS, and NV) is overestimated under WP3, WP4, WP5, and WP6, but there is a tendency to underestimate it under WP1 and WP2 of CFN1 (Figure 8c). This underestimation of the winds is at least partially related with the underestimation of the pressure differences over the Ebro Valley (Figure 5b) as a consequence of the initial and boundary conditions errors that occur in CFN1 (Figures 3a and 3c). CFN2 does not suffer from these initialization problems, and it shows an overestimation of the winds over the valleys in WP1 but still underestimates the winds over the valleys in WP2 (Figure 8d). Again, the numerical experiment CFN2.1 supports the relevance of the large errors introduced during the initialization process in CFN1 since the wind speed biases of CFN2.1 (not shown) are in agreement with CFN1 results (Figure 8c). This indicates that the propagation of errors from the synoptic scale to the regional scale can hamper potential improvements in the model formulation associated with the physics, for example. The underestimation of the winds under WP2 is partially related with the underestimation of the positive pressure gradient by CFN2 (Figure 5d) but also with a large underestimation of the wind speed at a few observational sites as it will be shown in the following lines.

[31] Figures 10 and 11 show the wind speed bias at the 41 observational sites calculated with the days belonging to

each one of the six WPs for CFN1 and CFN2, respectively. CFN1 shows a clear overestimation of the wind speed over the valleys and an underestimation at the sites located in mountain tops and the two hills for WP3–6 (Figures 10c–10f). This is in agreement with the pattern shown by the long-term wind speed biases (Figure 6a). The structure is less clear in WP1, which shows an underestimation of the wind in the southern part of the region, the Ebro Valley (Figure 10a). To a lesser extent this is also evident in WP2 (Figure 10b). These two WPs are, however, affected by the initial and boundary conditions problem of CFN1. Indeed, CFN2 does not suffer from these errors and shows a similar structure of the wind speed bias for the six WPs, high wind speed bias over the valleys and low wind speed bias on the hill and the mountains (Figure 11). In spite of the similar structure of the wind speed biases (Figure 11), the wind speed tends to be underestimated in the EV (NS) subregion under WP1 and WP2 (WP2) (Figure 8d). This is a consequence of the influence exerted in the regional average by large underestimations at a few sites. The underestimation of the wind speeds at the hills (stations 7 and 8) is responsible for the slight underestimation of the wind at the EV subregion for WP1 and WP2 (Figures 11a and 11b) since when we exclude them from the calculation of the regional wind, the wind speed is no longer underestimated at the EV (bias is 0.56 and 0.03 for WP1 and WP2). Similarly, the underestimation of the wind speed at the NS subregion during WP2 is a result of the dominance of the high underestimation that occurs at station 14 (Figure 1). The station is located in a mountain pass that produces a local channeling that intensifies the northern winds. This significant topographic effect is not captured by WRF leading to the underestimation of the winds at this site (Figure 11b). Indeed, if station 14 is excluded in the calculation of the regional wind speed at the NS subregion, the wind is overestimated (bias is 0.46).

[32] The performance of the simulations to reproduce the observed wind is summarized in Figures 8e and 8f, which shows the averaged vectorial differences at the different WPs and subregions. The vectorial difference for each pair of observed simulated time series is defined as

$$\text{diff} = \frac{\sum_{i=1}^N \sqrt{(u_{\text{WRF}}(i) - u_{\text{obs}}(i))^2 + (v_{\text{WRF}}(i) - v_{\text{obs}}(i))^2}}{N}, \quad (1)$$

where u and v are the zonal and meridional wind components and N is the number of days under each WP. N is therefore different for each WP. A clear improvement of CFN2 in comparison with CFN1 can be appreciated in WP1 and WP2. The improvement is evident at the four regions. The improvement is mainly a consequence of the better initial and boundary conditions of CFN2 in comparison with CFN1 (Figure 3), more specifically, with the better simulation of the pressure gradient over the Ebro Valley (Figure 5). This better initialization produces improvements in both the wind direction and the wind speed in these two WPs (Figures 8a–8d) which ultimately reflect in the better scores shown here. The larger deviations are found for WP3 and WP5 (Figure 8f) due to the large overestimation of the wind speed over the valleys that occurs during these patterns (Figure 8b).

[33] To complete the analysis, it is interesting to discuss how CFN1 and CFN2 compare to ERA-40 and

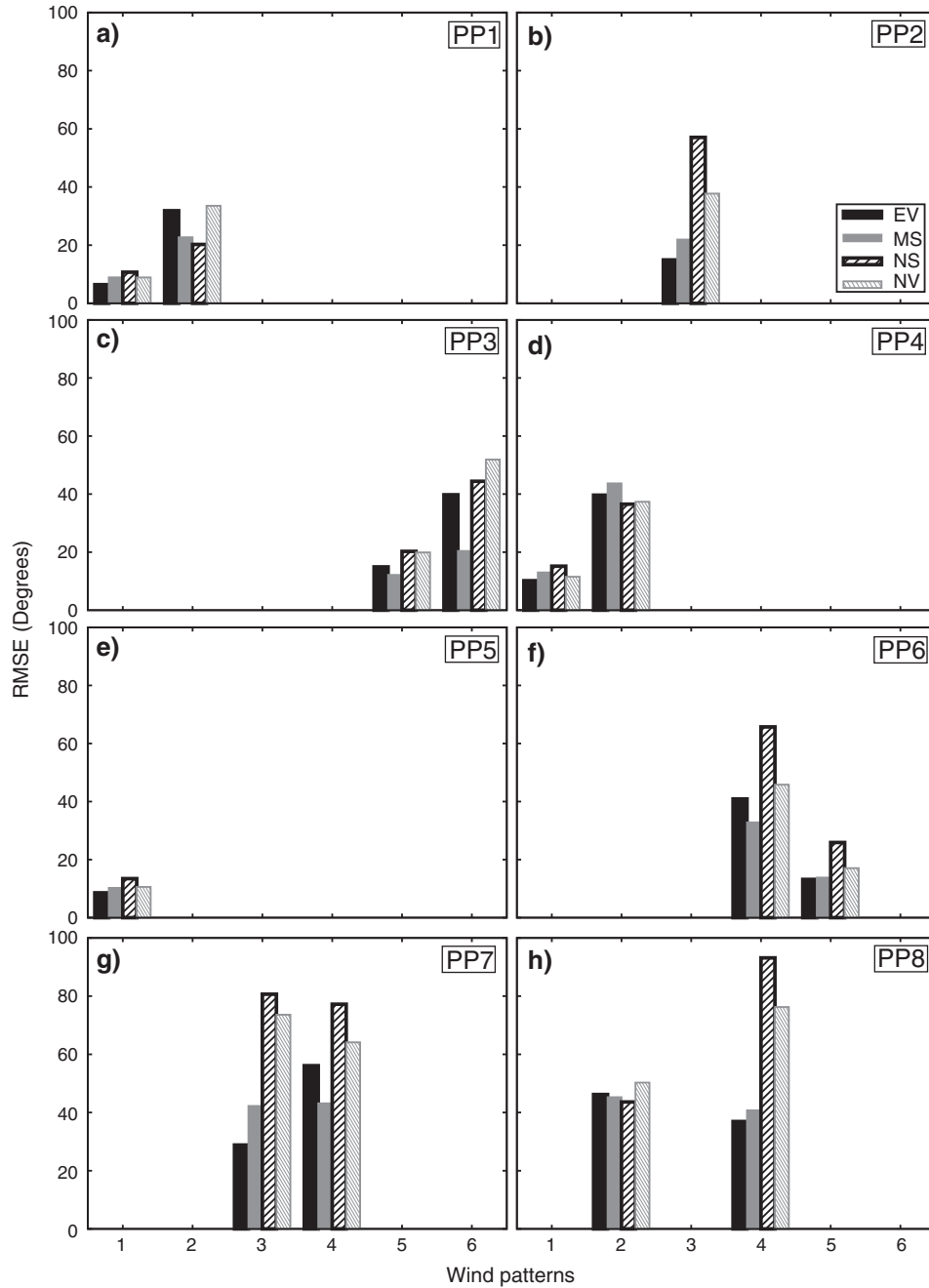


Figure 13. RMSE of the wind direction calculated with CFN2 and the observations at the different regions (see legend in Figure 13b) for the subsamples corresponding to the strongest associations between the PPs and the WPs. Each panel is associated with a particular PP (see labels).

ERA-Interim. The added value is quantified using the relative error of the averaged vectorial differences [equation (1)] calculated with the WRF simulations and the wind at 10 m from the ECMWF data sets, i.e.,

$$\text{diff}_{\text{rel}} = \frac{\text{diff}_{\text{WRF}} - \text{diff}_{\text{ECMWF}}}{\text{diff}_{\text{ECMWF}}}. \quad (2)$$

Results for each WP and wind region are shown in Figure 12. Both simulations show a clear added value with respect to the ECMWF reanalyses showing a reduction of the error of up to 60% for certain combinations of

WPs/wind regions. The adverse effect of the initialization problem of CFN1 is evident in the relative error of WP2 that shows a degradation of about 20% with respect to ERA-40 (Figure 12a). As previously discussed, CFN2 results are unaffected from the initialization problem and thus show a reduction of the error for this WP2 (Figure 12b). The EV and MS subregions show a reduction of the error for the six WPs. However, for NW winds, WP1–3 (SE winds, WP4–5), CFN2 tends to show a degradation with respect to ECMWF at the NV (NS) subregion. This indicates a directional dependency of the added value that WRF provides over complex terrain.

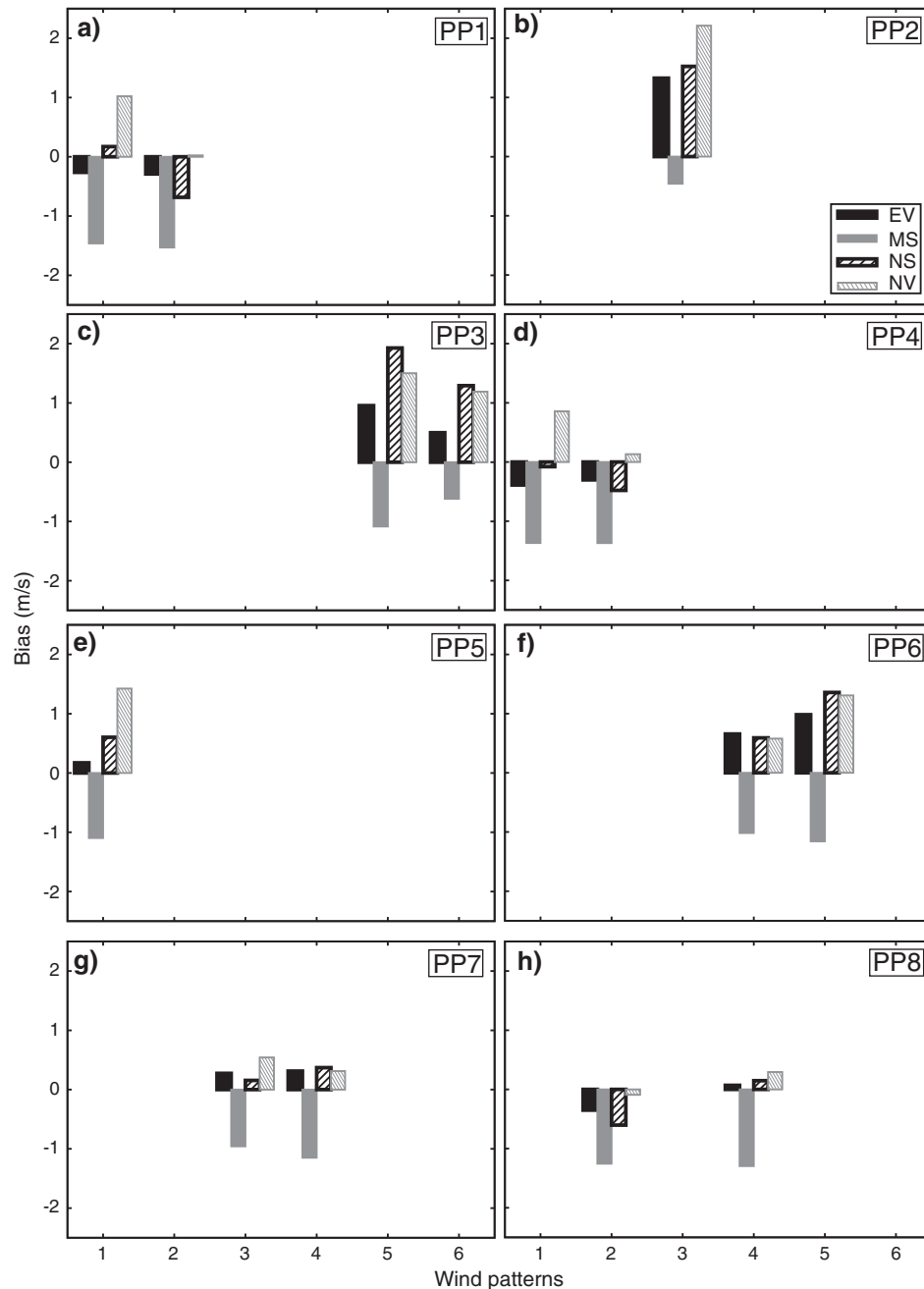


Figure 14. Wind speed biases (CFN2-observations) at the different regions (see legend in Figure 14b) for the subsamples corresponding to the strongest associations between the PPs and the WPs. Each panel is associated with a particular PP (see labels).

5. Large-Scale Influence on the Simulated Wind Field

[34] The influence of the synoptic scale situation in the wind field reproducibility is investigated in this section. The analysis consists of splitting the evaluation at the WPs for representative synoptic situations typical of the Iberian Peninsula, the eight PPs identified in JEA09. The PPs showed clear associations with the six WPs (Table 3 of JEA09). Hence, an evaluation of the wind field reproducibility as a function of representative large-scale situations can be obtained by analyzing the accuracy of the simulation to reproduce the WPs under their associated PPs. For this purpose, the RMSE of the direction, the wind speed bias,

and the mean wind differences are calculated for observations and simulation of days belonging to each one of these WP-PP associations. Four pairs of RMSE, bias, and vector differences are calculated within each association, one for each regional time series obtained as a result of averaging the wind information of stations classified under each wind subregion with different wind variability (Figure 1). Results using the simulated winds from CFN2 are shown in Figures 13, 14, and 15.

[35] The wind direction reproducibility shows an interesting relationship with the different WPs-PPs associations (Figure 13). The EV and the MS subregions are the ones that tend to show better scores under all the associations.

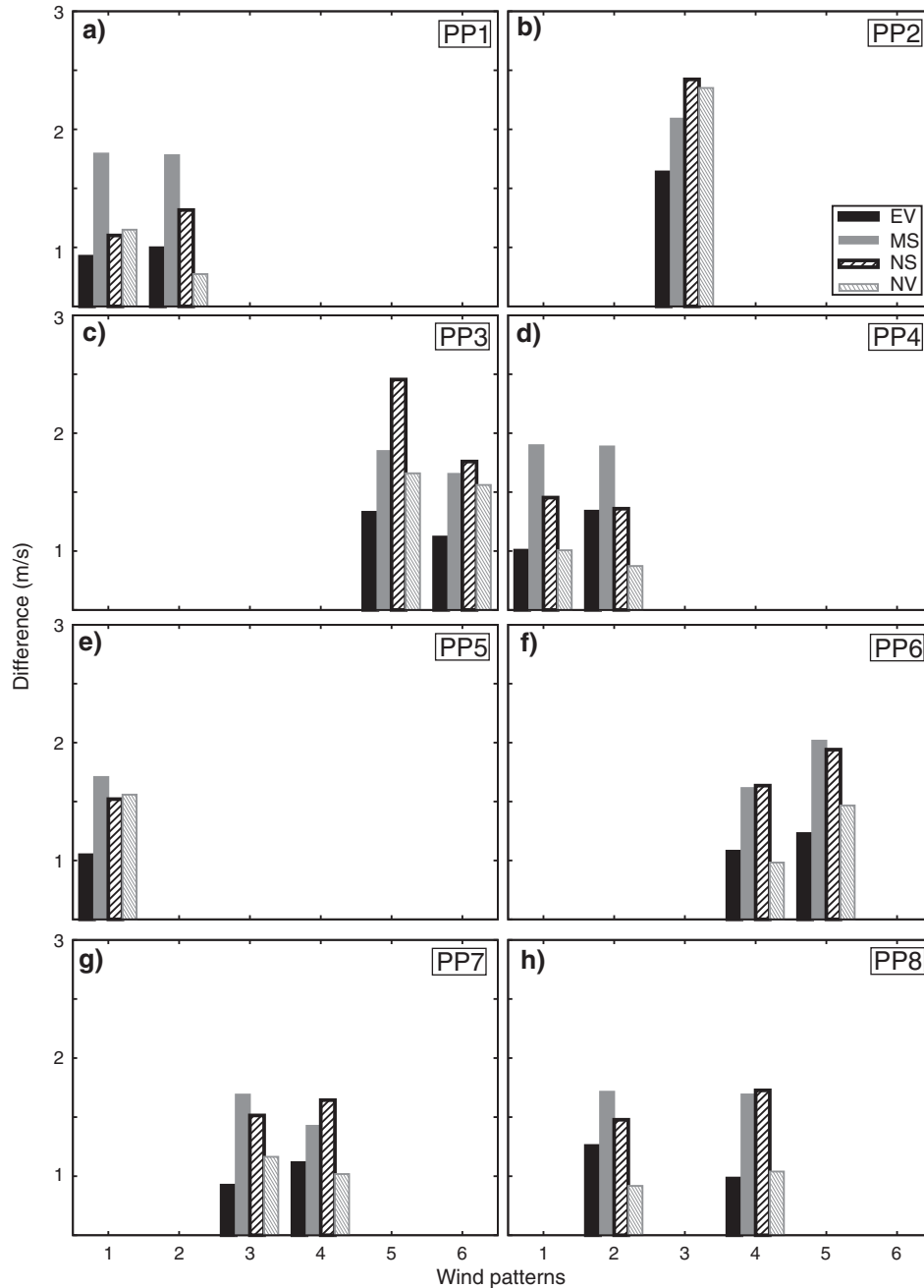


Figure 15. Vectorial wind differences (CFN2-observations) at the different regions (see legend in Figure 15b) for the subsamples corresponding to the strongest associations between the PPs and the WPs. Each panel is associated with a particular PP (see labels).

On the contrary, the most complex terrain regions, NS and NV, show the largest errors in the simulation of the wind direction. The reproducibility of a given WP does not show a strong dependence on the particular PPs that is producing the surface pattern. This is especially clear for WP1, WP5, or even WP2. WP4 reveals the largest sensitivity to the synoptic scale forcings.

[36] The underestimation of the wind speed at the mountain subregion is very systematic. All the associations between the WPs and the PPs show this negative bias (Figure 14). This reinforces the attribution of JD12 to the limitations in the representation of topography since the bias is independent of the structure of the flow (the WPs) or even

the synoptic situation (the PPs). The overestimation over the valleys is also very systematic between WP3–6 and all their associated PPs. This overestimation is less clear for WP1 and WP2. WP1 shows a certain dependence in the synoptic situation. The wind speed over the valleys is overestimated during PP5 (Figure 14e), but it shows a less clear structure, with underestimation at certain valley subregions and overestimation at other valleys, under PP1 and PP4 (Figures 14a and 14d). WP2 shows a clear underestimation of the wind over the valleys under its typical synoptic forcings PP1, PP4, and PP8 (Figures 14a, 14d, and 14h). This systematic underestimation of the wind at the valleys is partially originated by the underestimation of the wind at station 14 and

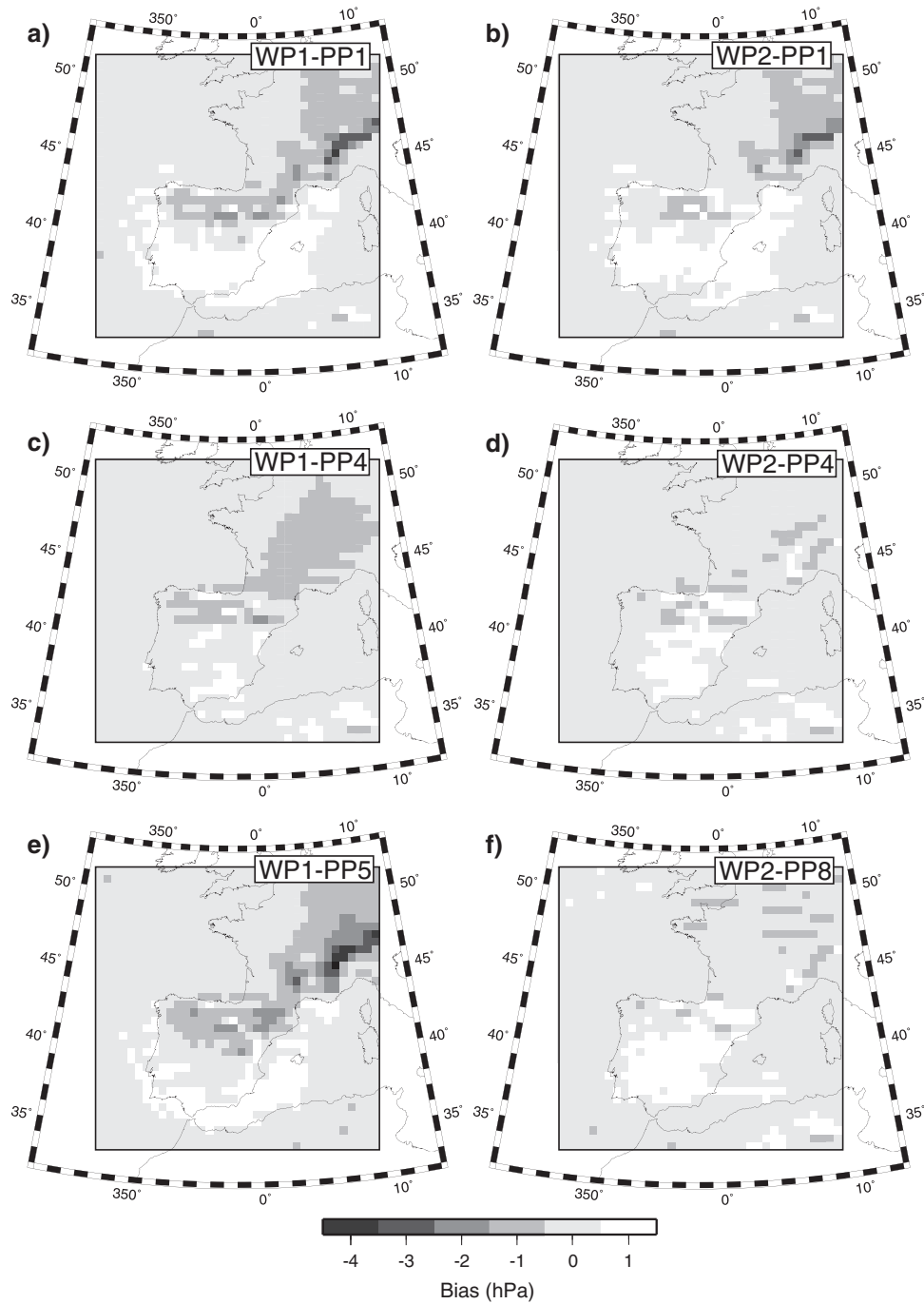


Figure 16. SLP biases calculated with CFN2 (outermost WRF domain) and ERA-Interim for different associations between the WPs and the PPs (see labels).

at the two hill stations in the broad Ebro Valley (see previous section). However, limitations in the reproduction of the synoptic scale situation are also responsible for this underestimation. This is illustrated with the SLP biases calculated with the associations between WP1 and WP2 and their PPs (Figure 16).

[37] The WP1-PP1 association shows a clear positive pressure bias over the Mediterranean Sea (Figure 16a). This bias leads to an underestimation of the pressure difference over the Ebro Valley of about 1 hPa, which is also responsible for the underestimation of the wind that occurs in the EV subregion during this association (Figure 14a). Roughly, the

northwestern wind speeds increase 10 m s^{-1} for a pressure difference of 20 hPa (Figure 2a), so an underestimation of 1 hPa produces an underestimation of the wind of 0.5 m s^{-1} . This underestimation indicates that the wind speed bias that occurs over the EV in WP1 (Figure 11a) would have been reversed if PP1 was appropriately reproduced by WRF. The SLP bias over the Mediterranean Sea is also present in the WP2-PP1 association (Figure 16b) which is also partially responsible for the underestimation of the wind over the valleys during this association (Figure 14a). The association WP1-PP5 shows a similar bias in the SLP field (Figure 16) that will indicate that a better simulation of the synoptic

situation by WRF would produce an even higher overestimation of the wind over the valleys (Figure 14e). The positive SLP bias can be speculated to be associated with the advection of air from the Atlantic to the Mediterranean Sea which in its pass through the Iberian Peninsula becomes too cold. The rest of the associations (WP1-PP4, WP2-PP4, and WP2-PP8) do not show biases in the calculation of the pressure difference over the Ebro Valley and west Mediterranean area (Figures 16c, 16d, and 16f). The underestimation of the regional wind in these situations is mainly associated with local underestimations such as over the hills and at the mentioned station 14.

[38] The mean wind differences summarize the ability of WRF to reproduce the surface wind field as a function of the synoptic scale situation (Figure 15). There is a rather systematic worse performance at the mountain subregion in comparison with the valley subregions in most of the WPs-PPs associations. The EV and the NV subregions in general show a better wind simulation than in the NS subregion, likely due to the more complicated topography of the last region. The worse performance is found for the WP3-PP2 (Figure 15b), WP5-PP3 (Figure 15c), and WP5-PP6 (Figure 15f) associations. These large errors arise mostly from the wind speed biases under these associations (Figures 14b, 14c, and 14f).

6. Conclusions

[39] By combining 13 year results of high spatial resolution numerical experiments with a dense network of surface wind observations, we deepen in our understanding of the ability of WRF to reproduce the surface wind over complex terrain. The evaluation herein presented consists of assessing the performance of the model under typical wind fields or WPs. This allows one to inspect the differentiated ability of the simulation to reproduce the different wind regimes over an area and thus evaluate the model's performance in terms of the direction of the flow. Our findings rely on the long time series and the high spatial coverage that enable us to become confident in the characterization of the model performance. The combination of an evaluation based on WPs with a classification of the synoptic patterns, the PPs in this investigation, further strengthen the advantages of these kinds of evaluations since it allows to robustly discriminate the model performance as a function of the synoptic situation too.

[40] The spatial structure of the flow of each WP is generally reproduced satisfactorily by WRF. This clearly shows the added value of the WRF simulations since the coarser horizontal resolution of the ECMWF data is unable to provide regional details of the wind at the meso-alpha and smaller spatial scales. The mountain sites and the plains show the best scores in the wind direction, whereas the sites located over valleys in more complex terrain regions show a worse performance. The wind speed is systematically underestimated at the sites located at mountain tops and hills, and it is overestimated at plains and valleys. This indicates that in spite of using high horizontal resolutions, care needs to be taken in using a wind simulation as substitute of the real world over complex terrain. The biases were attributed by JD12 to limitations of the horizontal resolution used in the simulation, 2 km, to reproduce the topographic features over

the region. However, JD12 did not consider the differential effects of the wind direction and the large-scale situation in their investigation. The fact that the biases are systematic under different directions of the flow and different synoptic situations found in this study confer more credibility to the attribution of the wind speed biases to the topographic misrepresentation. An appropriate representation of the effects produced by the unresolved topography, in line with the ideas of the parameterization of JD12 for instance, becomes necessary in order to improve the WRF model performance in reproducing the surface wind observations. Actually, an inspection of the parameterization of the transport of momentum within the whole planetary boundary layer would be helpful to understand the origin of potential misrepresentations near the surface.

[41] Potential errors at the synoptic scale arising during the initialization procedure may introduce important deviations from the observed wind behavior (e.g., CFN1). This result goes beyond an initialization problem, stressing that uncertainties at the synoptic scale propagate to the regional scale being responsible for large misrepresentations. Similar errors to the ones herein found could be introduced by the physics of the models that, for instance, can be responsible for the underestimation of the intensity of high-pressure systems. Errors in the synoptic scale can also originate in the boundary conditions and propagate to the regional scale. This indicates sensitivity to the domain size. A large domain can help to reduce the uncertainty introduced by the boundary conditions on the regional scale of interest. An improved initialization (CFN2) indicates that, in general, errors in the surface wind simulation do not show a strong dependence in the synoptic pattern, the PPs in this case. However, some biases were identified. The SLP over the Mediterranean Sea is overestimated under certain synoptic situations by about 1 hPa, which produces weaker simulated winds over the region than would have been expected by an adequate representation of the large scale. This further reflects the propagation of uncertainties from larger to smaller atmospheric scales of motion. The SLP underestimation produces in some days the simulation of circulations with opposite sense to the observed one. These results show the strong influence that the large scale exerts over the surface winds and suggest that the potential improvement obtained in the downscaling by increasing the horizontal resolution may be hampered if the large scale is not appropriately captured.

[42] **Acknowledgments.** This investigation was partially supported by projects CGL-2008-05093/CLI and CGL-2011-29677-C02 and was accomplished within the collaboration agreement 09/490 between CIEMAT and NCAR as well as the collaboration agreement 09/153 between CIEMAT and UCM. NCAR is sponsored by the National Science Foundation. We would like to thank the Navarra government and the ECMWF for facilitating the access to its data sets. We also would like to thank the reviewers for their constructive comments which helped to increase the value of the contents of the manuscript.

References

- Black, T. L. (1994), The new NMC mesoscale Eta Model: Description and forecast examples, *Wea. Forecasting*, 9, 265–278.
- Buckley, R. L. (2004), Statistical comparison of Regional Atmospheric Modelling System forecasts with observations, *Meteorol. Appl.*, 11, 67–82.
- Conil, S., and A. Hall (2006), Local regimes of atmospheric variability: A case study of southern California, *J. Clim.*, 19, 4308–4325.

- Cotton, W. R., et al. (2003), RAMS 2001: Current status and future directions, *Meteorol. Z.*, **82**, 5–29.
- Cox, R., B. L. Bauer, and T. Smith (1998), A mesoscale model intercomparison, *Bull. Am. Meteorol. Soc.*, **79**, 265–283.
- Darby, L. S. (2005), Cluster analysis of surface winds in Houston, Texas, and the impact of wind patterns on ozone, *J. Appl. Meteorol.*, **44**, 1788–1806.
- Dee, D. P., et al. (2011), The ERA-Interim reanalysis: Configuration and performance of the data assimilation system, *Quarter. J. R. Meteorolog. Soc.*, **137**, 553–597.
- DeGaetano, A. T. (1996), Delineation of mesoscale climate zones in the northeastern United States using a novel approach to cluster analysis, *J. Clim.*, **9**, 1765–1782.
- Fiebrich, C. A., C. R. Morgan, and A. G. McCombs (2010), Quality assurance procedures for mesoscale meteorological data, *J. Atmos. Oceanic Technol.*, **27**, 1565–1582.
- García-Bustamante, E., J. F. González-Rouco, P. A. Jiménez, J. Navarro, and J. P. Montávez (2008), The influence of the Weibull assumption in monthly wind energy estimation, *Wind Energy*, **11**, 483–502.
- García-Bustamante, E., J. F. González-Rouco, P. A. Jiménez, J. Navarro, and J. P. Montávez (2009), A comparison of methodologies for monthly wind energy estimations, *Wind Energy*, **12**, 640–659.
- Gillette, D. A., and K. J. Hanson (1989), Spatial and temporal variability of dust production caused by wind erosion in the United States, *J. Geophys. Res.*, **94**(D2), 2197–2206.
- Grell, G. A., J. Dudhia, and D. R. Stauffer (1994), A description of the fifth-generation Penn State/NCAR Mesoscale Model (MM5). *NCAR Tech. Note NCAR/TN-398 1 STR*.
- Hanna, S. R., and R. Yang (2001), Evaluations of mesoscale models' simulations of near-surface winds, temperature gradients and mixing depths, *J. Appl. Meteorol.*, **40**, 1095–1104.
- Jiménez, P. A., and J. Dudhia (2012), Improving the representation of resolved and unresolved topographic effects on surface wind in the WRF model, *J. Appl. Meteor. & Climatol.*, **51**, 300–316.
- Jiménez, P. A., J. Dudhia, J. F. González-Rouco, J. Navarro, J. P. Montávez, and E. García-Bustamante (2012), A revised scheme for the WRF surface layer formulation, *Mon. Wea. Rev.*, **140**, 898–918.
- Jiménez, P. A., J. F. González-Rouco, J. P. Montávez, J. Navarro, E. García-Bustamante, and J. Dudhia (2013), Analysis of the long-term surface wind variability over complex terrain using a high spatial resolution WRF simulation, *Clim. Dyn.*, **40**, 1643–1656, doi:10.1007/s00382-012-1326-z.
- Jiménez, P. A., J. F. González-Rouco, E. García-Bustamante, J. Navarro, J. P. Montávez, J. Vilà-Guerau de Arellano, J. Dudhia, and A. Roldán (2010a), Surface wind regionalization over complex terrain: Evaluation and analysis of a high resolution WRF numerical simulation, *J. Appl. Meteor. & Climatol.*, **49**, 268–287.
- Jiménez, P. A., J. F. González-Rouco, J. P. Montávez, E. García-Bustamante, and J. Navarro (2009), Climatology of wind patterns in the northeast of the Iberian Peninsula, *Int. J. Climatol.*, **29**, 501–525.
- Jiménez, P. A., J. F. González-Rouco, J. P. Montávez, J. Navarro, E. García-Bustamante, and F. Valero (2008), Surface wind regionalization in complex terrain, *J. Appl. Meteor. & Climatol.*, **47**, 308–325.
- Jiménez, P. A., J. F. González-Rouco, J. Navarro, J. P. Montávez, and E. García-Bustamante (2010b), Quality assurance of surface wind observations from automated weather stations, *J. Atmos. Oceanic Technol.*, **27**, 1101–1122.
- Kaufmann, P., and C. D. Whiteman (1999), Cluster-analysis classification of wintertime wind patterns in the Grand Canyon region, *J. Appl. Meteor.*, **38**, 1131–1147.
- McVicar, T. R., et al. (2012), Global review and synthesis of trends in observed terrestrial near-surface wind speeds: Implications for evaporation, *J. Hydrology*, **416–417**, 182–205.
- Mesinger, F., et al. (2006), North American regional reanalysis, *Bull. of the Amer. Met. Soc.*, **87**, 343–360.
- Mesinger, F., R. L. Wobus, and M. E. Baldwin (1996), Parameterization of form drag in the Eta Model at the National Centers for Environmental Prediction, in *Preprints, 11th Conf. on Numerical Weather Prediction*, Amer. Met. Soc., Norfolk, VA, 324–326.
- Miao, J.-F., D. Chen, K. Wyser, K. Borne, J. Lindgren, M. K. S. Strandvall, S. Thorsson, C. Achberger, and E. Almkvist (2008), Evaluation of MM5 mesoscale model at local scale for air quality applications over the Swedish west coast: Influence of PBL and LSM parameterizations, *Meteor. Atmos. Phys.*, **99**, 77–103.
- Oreskes, N. (1998), Evaluation (not validation) of quantitative models, *Environ Health Perspect.*, **106**, 1453–1459.
- Oreskes, N., K. Shrader-Frechette, and K. Belitz (1994), Verification, validation, and confirmation of numerical models in the earth sciences, *Science*, **263**, 641–646.
- Palutikof, J. P., P. M. Kelly, T. D. Davies, and J. A. Halliday (1987), Impacts of spatial and temporal wind speed variability on wind energy output, *J. Appl. Meteor.*, **26**, 1124–1133.
- Pielke, R. A. (2002), *Mesoscale Meteorological Modeling*, 676 pp, Academic Press, San Diego, CA.
- Pryor, S. C., R. J. Barthelmie, and E. Kjellström (2005), Potential climate change impact on wind energy resources in northern Europe: Analyses using a regional climate model, *Clim. Dyn.*, **25**, 815–835.
- Reid, S., and R. Turner (2001), Correlation of real and model wind speeds in different terrains, *Wea. Forecasting*, **16**, 620–627.
- Rife, D. R., C. A. Davis, Y. Liu, and T. T. Warner (2004), Predictability of low-level winds by mesoscale meteorological models, *Mon. Wea. Rev.*, **132**, 2533–2569.
- Romero, R., G. Summer, C. Ramis, and A. Genovés (1999), A classification of the atmospheric circulation patterns producing significant daily rainfall in the Spanish Mediterranean area, *Int. J. Climatol.*, **19**, 765–785.
- Rontu, L. (2006), A study on parameterization of orography-related momentum fluxes in a synoptic-scale NWP model, *Tellus*, **58A**, 69–81.
- Skamarock, W. C., J. B. Klemp, J. Dudhia, D. O. Gill, D. M. Barker, M. Duda, X.-Y. Huang, W. Wang, and J. G. Powers (2008), A description of the advanced research WRF version 3. *Technical Report TN-475+STR*, NCAR.
- Skamarock, W. C., J. B. Klemp, J. Dudhia, D. O. Gill, D. M. Barker, W. Wang, and J. G. Powers (2005), A description of the advanced research WRF Version 2. *Technical Report TN-468+STR*, NCAR.
- Uppala, S. M., et al. (2005), The ERA-40 re-analysis, *Quarter. J. Roy. Met. Soc.*, **131**, 2961–3012.
- von Storch, H. (1995), Inconsistencies at the interface of climate impact studies and global climate research, *Meteorol. Z.*, **4 NF**, 72–80.
- Walter, A., K. Keuler, D. Jacob, R. Knoche, A. Block, S. Kotlarski, G. Müller-Westermeier, D. Rechid, and W. Ahrens (2006), A high resolution data set of German wind velocity 1951–2001 and comparison with regional climate model results, *Meteorol. Z.*, **15**, 585–596.
- White, D., M. Richman, and B. Yarnal (1991), Climate regionalization and rotation of principal components, *Int. J. Climatol.*, **11**, 1–25.
- Whiteman, C. D. (2000), *Mountain Meteorology: Fundamentals and Applications*, 355 pp, Oxford University Press, New York, New York.
- Zagar, N., M. Zagar, J. Cedilnik, G. Gregoric, and J. Rakovec (2006), Validation of mesoscale low-level winds obtained by dynamical downscaling of ERA40 over complex terrain, *Tellus*, **58A**, 445–455.